

# Flux Linkage-Based Model Predictive Current Control for Nonlinear PMSM Drives

Sebastian Wendel\*, Petros Karamanakos†, Armin Dietz\*, Ralph Kennel‡

\*Institute ELSYS, Technische Hochschule Nuernberg, 90489 Nuremberg, Germany

Email: \*sebastian.wendel@th-nuernberg.de, armin.dietz@th-nuernberg.de

†Faculty of Information Technology and Communication Sciences, Tampere University, 33101 Tampere, Finland

Email: †p.karamanakos@ieee.org

‡Chair of Electrical Drive Systems and Power Electronics, Technical University of Munich, 80333 Munich, Germany

Email: ‡ralph.kennel@tum.de

**Abstract**—In this paper, a flux linkage-based direct model predictive current control approach is presented for small permanent magnet synchronous motor (PMSM) drives. The method aims to minimize the current ripples at steady state by deciding on the optimal switching instant, while exhibiting fast dynamic behavior during transients. To this end, the future trajectory of the stator current is not computed based on the machine inductances or inductance look-up tables, but on the changes of the magnetic flux linkage by utilizing flux linkage maps. As shown, the proposed method can be particularly advantageous for electric drives with a noticeable nonlinearity in terms of saturation and/or cross-coupling effects since it allows for a significantly increased prediction accuracy, which leads to an improved steady-state performance as indicated by the reduced current distortions.

## I. INTRODUCTION

Finite control set model predictive control (FCS-MPC), also known as direct model predictive control (DMPC), addresses the control and modulation problems in one computational stage. Specifically, a cost function that quantifies the control objectives is minimized subject to explicit constraints. The discrete voltage space vector (SV) that solves the optimization problem underlying FCS-MPC is the optimal one and is directly applied to the power electronic converter. Thanks to its optimal nature, FCS-MPC can achieve favorable steady-state performance, while its direct control nature allows for very fast transient responses.

The main challenge most FCS-MPC algorithms face relates to their computational complexity. Even though there are powerful computational platforms, such as system-on-a-chip field-programmable gate arrays (SoC FPGAs), readily available that facilitate the real-time implementation of FCS-MPC for sampling/control frequencies  $f_{cf}$  of several hundred kHz [1], an as high sampling frequency as possible is required to ensure a fine granularity of switching [2]. This need is even more prominent when power electronic systems with time constants of just a few ms—or even  $\mu$ s—are of concern. Such systems, as small electrical drives, operate at relatively high switching frequencies; given that in FCS-MPC the sampling frequency should be about two orders of magnitude higher

than the average switching frequency [2], it can be understood that a very high  $f_{cf}$  is required.

To address the above issue, some strategies that introduce a variable switching point (VSP), i.e., a (switching) time instant within the control interval at which a new voltage SV is applied to the converter, have been presented, see, e.g., [3]–[7]. These methods aim to combine the high granularity of modulation-based methods, such as carrier-based pulse width modulation (CB-PWM), while still keeping their direct-control characteristics. In doing so, ripples in the output variables, e.g., the stator current or the electromagnetic torque, are reduced.

However, all previous VSP predictive current control (VSP<sup>2</sup>CC) approaches compute the future current trajectory—and thus the VSP—based on the (absolute) inductances of the system. When interior permanent magnet synchronous motors (IPMSMs) are of concern, the absolute inductances  $L_d$  and  $L_q$  can describe the basic dynamics of the drive system. However, the ever-increasing demand for highly utilized IPMSMs with reduced manufacturing costs and weight results in the design of IPMSMs which exhibit saturation effects already within the nominal operation range [8]. This, combined with the existing cross-coupling effects motivated the introduction of differential inductances  $L_{dd}$ ,  $L_{dq}$ ,  $L_{qq}$ , and  $L_{qd}$ , for higher modeling accuracy [9]. Using a prediction model based on the four inductances, however, complicates the system modeling and increases the computational effort. Moreover, due to their dependency on current changes, they are susceptible to noise-contaminated current measurements during their estimation.

For the aforementioned reasons, this work proposes to compute the current behavior based on flux linkage maps. In doing so, the computational load of MPC can be kept modest, while a more accurate current prediction can be made; the flux linkage maps can be easily determined based on the steady-state voltage equation of the PMSM using the (online tracked) resistance along with current and voltage measurements, averaged—thus filtered—over several samples and motor shaft revolutions. Thus, the computation of the current gradients, which are required for calculating the VSPs in VSP<sup>2</sup>CC can be carried out more precisely. As shown, the presented flux linkage-based VSP<sup>2</sup>CC approach can significantly reduce the total harmonic distortion (THD) of the stator current as compared with an inductance-based VSP<sup>2</sup>CC.

The research leading to these results has received funding from the Bavarian Ministry of Economic Affairs, Energy and Technology and is managed by VDI/VDE under grant agreement ESB048/004.

## II. CONTROL MODEL

The proposed flux linkage-based VSP<sup>2</sup>CC approach is implemented for a three-phase two-level voltage source inverter (VSI) and both surface PMSMs (SPMSMs) and IPMSMs. Saturation and cross-coupling are taken into account.

### A. Nonlinear Model of the Drive System

The continuous-time controlled system is described by

$$\mathbf{v}_{dq}(t) = R_{ph}(\vartheta)\mathbf{i}_{dq}(t) + \frac{d\boldsymbol{\psi}_{dq}(t)}{dt} + \omega_{el}(t)\mathbf{Q}\boldsymbol{\psi}_{dq}(t) \quad (1)$$

where  $\mathbf{v}_{dq} = [v_d \ v_q]^T$  and  $\mathbf{i}_{dq} = [i_d \ i_q]^T$  are the stator voltage and current, respectively, and  $R_{ph}$  the stator resistance, which depends on the winding temperature  $\vartheta$ . Moreover,  $\boldsymbol{\psi}_{dq} = [\psi_d \ \psi_q]^T$  is the flux linkage, with  $\psi_d(t) = \psi_d^*(t) + \psi_{PM}(\varphi, \vartheta_m)$  and  $\psi_{PM}$  being the permanent magnet flux constant, while  $\omega_{el}$  the electrical angular speed. Finally,  $\mathbf{Q} = \begin{bmatrix} 0 & -1 \\ 1 & 0 \end{bmatrix}$ . Note that the flux linkages on the d- and q-axis depend on the respective currents and the rotor position  $\varphi$ , whereas the permanent magnet flux linkage  $\psi_{PM}$  varies with the magnet temperature  $\vartheta_m$ . Moreover, (1) accounts for effects such as saturation and cross-coupling, which in the case of highly utilized synchronous machines should not be neglected. Specifically, the flux linkage changes are given by [9], [10],

$$\Delta\psi_d = \frac{d\psi_d(t)}{dt} = \underbrace{\frac{\partial\psi_d^*}{\partial i_d}}_{L_{dd}} \frac{di_d(t)}{dt} + \underbrace{\frac{\partial\psi_d^*}{\partial i_q}}_{L_{dq}} \frac{di_q(t)}{dt} + \underbrace{\frac{\partial\psi_d}{\partial\varphi}}_{\Lambda_d \approx 0} \underbrace{\frac{d\varphi(t)}{dt}}_{\omega_{el}(t)} \quad (2a)$$

$$\Delta\psi_q = \frac{d\psi_q(t)}{dt} = \underbrace{\frac{\partial\psi_q}{\partial i_q}}_{L_{qq}} \frac{di_q(t)}{dt} + \underbrace{\frac{\partial\psi_q}{\partial i_d}}_{L_{qd}} \frac{di_d(t)}{dt} + \underbrace{\frac{\partial\psi_q}{\partial\varphi}}_{\Lambda_q \approx 0} \underbrace{\frac{d\varphi(t)}{dt}}_{\omega_{el}(t)}. \quad (2b)$$

In the sequel of this paper, the proposed MPC algorithm utilizes a flux linkage-based prediction model derived from the aforementioned equations. To this aim, the permanent magnet and resistance temperatures are regularly updated based on the system time constant. However, any variations in the flux linkage due to the rotor position dependency are neglected; the corresponding flux linkage maps would be four dimensional (4D), thus difficult to utilize in real time, and the resulting prediction error is small and, thus, acceptable [10, p. 25]. Also, it is worth mentioning that identifying the rotor position dependency with acceptable effort is rather challenging. Finally, the adverse effects of manufacturing imperfections that can potentially lead to a nonuniform air-gap field are considered—within a small tolerance band—negligible [11].

### B. Inductance-Based Prediction Model

Most commonly, the evolution of the stator current is of interest when FCS-MPC algorithms for PMSM drive systems are of concern. The predicted current is computed by discretizing (1) and (2) based on forward Euler discretization [1], i.e.,

$$\mathbf{i}_{dq}(k+1) = T_{cf}\mathbf{L}^{-1} \left( \mathbf{v}_{dq}(k) - R_{ph}\mathbf{i}_{dq}(k) - \omega_{el}(k) \left( \mathbf{Q}\mathbf{L}\mathbf{i}_{dq}(k) + \begin{bmatrix} 0 \\ \psi_{PM} \end{bmatrix} \right) \right) + \mathbf{i}_{dq}(k) \quad (3)$$

where  $T_{cf}$  is the sampling interval and  $\mathbf{L} = \text{diag}(L_d, L_q)$ . As can be seen in (3), the predicted current  $\mathbf{i}_{dq}(k+1)$  depends on the (time-varying) absolute inductances  $L_d$  and  $L_q$ . Hence, assuming constant inductances leads to less accurate predictions and, consequently, to potential performance deterioration.

### C. Flux Linkage-Based Prediction Model

To address the previous issue, in this section a flux linkage-based prediction model is presented. Using forward Euler discretization, the voltage equation (1) gives

$$\mathbf{v}_{dq}(k) = R_{ph}\mathbf{i}_{dq}(k) + \frac{\Delta\boldsymbol{\psi}_{dq}(k+1)}{T_{cf}} + \frac{1}{2}\omega_{el}\mathbf{Q}\boldsymbol{\psi}_{dq}(k+1) \quad (4)$$

where  $\Delta\boldsymbol{\psi}_{dq}(k+1) = \boldsymbol{\psi}_{dq}(k+1) - \boldsymbol{\psi}_{dq}(k)$  and  $\boldsymbol{\psi}_{dq}(k+1) = \boldsymbol{\psi}_{dq}(k) + \boldsymbol{\psi}_{dq}(k+1)$ . Assuming a constant current for  $R_{ph}$  during  $T_{cf}$ , the flux linkage change at time step  $k+1$  is given by [8]

$$\boldsymbol{\psi}_{dq}(k+1) = \boldsymbol{\psi}_{dq}(k) + \frac{T_{cf}(\mathbf{v}_{dq}(k) - R_{ph}\mathbf{i}_{dq}(k) - \omega_{el}\mathbf{Q}\boldsymbol{\psi}_{dq}(k))}{1 + \frac{1}{4}T_{cf}^2\omega_{el}^2} - \frac{\frac{1}{2}T_{cf}^2\omega_{el}(\mathbf{Q}\mathbf{v}_{dq}(k) - R_{ph}\mathbf{Q}\mathbf{i}_{dq}(k) + \omega_{el}\boldsymbol{\psi}_{dq}(k))}{1 + \frac{1}{4}T_{cf}^2\omega_{el}^2}. \quad (5)$$

To simplify (5), the following assumptions are made. First, given that  $T_{cf} \ll 1$ , the last term of (5) can be neglected, since  $T_{cf}^2\omega_{el,\max} \approx 0$ . Second, it is assumed that  $\omega_{el,\max}^2 T_{cf}^2 \ll 1$ , where  $\omega_{el,\max}$  is the maximal possible angular speed.<sup>1</sup> Third, the rotor speed is assumed to remain constant within the prediction window of a few time steps  $T_{cf}$ .<sup>2</sup> Based on the above-mentioned assumptions, and after rearranging terms, (5) becomes

$$\boldsymbol{\psi}_{dq}(k+1) \approx \boldsymbol{\psi}_{dq}(k) + T_{cf} \frac{\mathbf{v}_{dq}(k) - R_{ph}\mathbf{i}_{dq}(k) - \omega_{el}\mathbf{Q}\boldsymbol{\psi}_{dq}(k)}{1 + \frac{1}{4}T_{cf}^2\omega_{el}^2} \quad (6)$$

Note that the above expression is also used for compensating for the delay time, i.e., the time between the measurements occur and the execution of the control action, caused by the real-time system.

## III. FLUX LINKAGE-BASED DIRECT MODEL PREDICTIVE CURRENT CONTROL WITH VARIABLE SWITCHING POINT

VSP<sup>2</sup>CC aims to reduce the current ripples while achieving excellent dynamic behavior, as explained in [7]. The proposed flux linkage-based modification allows this also for nonlinear machines. To this end, it decides in real time whether one full SV (similar to the classical FCS-MPC) or a VSP with a combination of two SVs is selected. Algorithm 1 shows the pseudocode of the discussed MPC method.

<sup>1</sup>It is important to mention, however, that even though the term  $\omega_{el,\max}^2 T_{cf}^2$  in most cases is almost zero, at very high speeds and low sampling/control frequencies (e.g.,  $\omega_{el}=1000$  rps and  $T_{cf}=1$  ms) it cannot be neglected.

<sup>2</sup>The speed, and consequently the term  $\omega_{el}^2 T_{cf}^2$ , are updated in a multiple of  $T_{cf}$ , based on the slower outer speed loop (see Section IV-B).

### A. Pre-selection Based on the Dead-Beat Control Action

First, a pre-selection method—introduced as “heuristic pre-selection” in [4]—which utilizes the deadbeat control action is adopted to minimize the computational burden. [4] and [7] describe in detail how the angle

$$\gamma(k) = \arctan 2(\mathbf{v}_{dq,db}(k)) + \varphi, \{\gamma \in \mathbb{R} | 0 \leq \gamma < 2\pi\} \quad (7)$$

of the desired deadbeat voltage vector  $\mathbf{v}_{dq,db}(k)$ , that drives the current to its reference, reduces the search space from eight candidate SVs to four. With (7), the triangular sector (one out of the six) wherein  $\mathbf{v}_{dq,db}(k)$  lies can be found. Moreover, for achieving lower switching frequency (and thus switching losses), while keeping the computational burden modest, the reference tracking error term is calculated only for one zero SV ( $sv_0$ ), whereas the switching error term considers both  $sv_0$  and  $sv_7$ . Subsequently, the zero SV that results in less switching effort—with respect to the previously applied SV—will be chosen. Thus, only the two active and zero SVs that form the sector are candidate solutions for the subsequent MPC problem.<sup>3</sup>

### B. VSP<sup>2</sup>CC Principle

The proposed algorithm evaluates the stator current evolution for the possible combinations of the three/four candidate SVs within a horizon of  $N_p$  steps. Specifically, there are two possibilities that are considered for the first prediction step, i.e., either one SV is applied to the inverter for the whole  $T_{cf}$  (i.e., similar to the conventional FCS-MPC), or two SVs are implemented within one  $T_{cf}$ , in line with the principles of VSP<sup>2</sup>CC. In addition, for prediction steps  $N_p > 1$ , standard FCS-MPC is employed, meaning that only three/four candidate solutions are considered from the second step of the horizon onwards, see Algorithm 1.

Since for VSP<sup>2</sup>CC the slopes of  $i_d$  and  $i_q$  are necessary, see [3], [4], these need to be computed. Before doing so, the following assumptions are made:

- The current slopes are assumed to be linear and insensitive to saturation within one  $T_{cf}$ .<sup>4</sup>
- The rotor angle  $\varphi$  is considered to be constant during one interval  $T_{cf}$ , as explained in [7].
- The current slopes are not affected by nonlinear time-varying parameters, such as  $R_{ph}$ ,  $\psi_{PM}$  and  $\omega_{el}$ , over one  $T_{cf}$  due to their significantly slower dynamics.

With the above assumptions, the (three possible) current slopes over one  $T_{cf}$  are given by

$$\mathbf{m}_{dq}(k) = \frac{\mathbf{i}_{dq}(k+1) - \mathbf{i}_{dq}(k)}{T_{cf}} = \frac{\Delta \mathbf{i}_{dq}(k)}{T_{cf}}. \quad (8)$$

Moreover, owing to these assumptions, the same slopes are assumed at time steps  $k$  and  $k+1$ . By denoting these slopes with the subscripts  $n_1$  and  $n_2$ , respectively, the rms current error on the d- and q-axis can be calculated over the entire period  $T_{cf}$  with [4]

<sup>3</sup>Note that even though such a method is prone to suboptimality [2], the results acquired with the proposed method, see Section IV, do not sacrifice optimality.

<sup>4</sup>If the used IPMSM has a noticeable saturation effect during one  $T_{cf}$ , this assumption is dropped, and the adopted approach is refined.

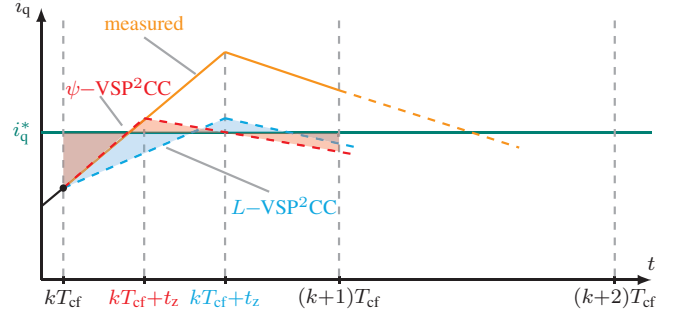


Figure 1. Flux linkage- and inductance-based VSPs  $t_z$  by the intersection of two  $i_q$  gradients. The measured current is obtained when L-VSP<sup>2</sup>CC is used while saturation occurs. For simplicity only  $i_q$  is shown.

$$e_{\text{rms}^2, n_1, n_2}(t_z) = \frac{1}{T_{cf}} \left( \int_0^{t_{z, n_1, n_2}} \|\mathbf{i}_{dq,0} + \mathbf{m}_{dq, n_1} t - \mathbf{i}_{dq}^*\|_2^2 dt + \int_{t_{z, n_1, n_2}}^{T_{cf}} \|\mathbf{i}_{dq, t_z} + \mathbf{m}_{dq, n_2} t - \mathbf{i}_{dq}^*\|_2^2 dt \right). \quad (9)$$

The variable switching point  $t_{z, n_1, n_2}$ , which leads to the minimum current ripple for each SV combination, is calculated by setting the derivative of (9) to zero, i.e.,  $de_{\text{rms}^2}/dt_z = 0$ . This yields

$$t_{z, n_1, n_2} = T_{cf} \frac{a_{n_1, n_2} + b_{n_1, n_2}}{c_{n_1, n_2} + d_{n_1, n_2}} \quad (10)$$

where the terms  $a_{n_1, n_2}$ ,  $b_{n_1, n_2}$ ,  $c_{n_1, n_2}$ , and  $d_{n_1, n_2}$  can be found in [7]. When the SVs at  $k$  and  $k+1$  are the same, the SV will be applied for the full interval  $T_{cf}$  ( $t_{z, n_1, n_2} = 0$ ). This implies that either one or zero (in case the SV applied at  $k$  is the same as the previously applied one, i.e., the one applied at  $k-1$ ) switching transitions occur within one  $T_{cf}$ . Finally, SV combinations that result in current gradients that do not intersect at all within  $T_{cf}$  or lead to  $t_{z, n_1, n_2} > T_{cf}$  are excluded as infeasible.

### C. Flux Linkage-Based Gradient Calculation

In this work, and in contrast to [7], the flux linkage is used for the current prediction. To this end, the following expressions are utilized

$$f_\psi : \mathbb{R}^2 \rightarrow \mathbb{R}^2, (i_d, i_q) \rightarrow (\psi_d, \psi_q) \quad (11a)$$

$$f_\psi^{-1} : \mathbb{R}^2 \rightarrow \mathbb{R}^2, (\psi_d, \psi_q) \rightarrow (i_d, i_q). \quad (11b)$$

First, (11a) is used to map the current  $\mathbf{i}_{dq}(k+\ell-1)$ , with  $\ell = 1, \dots, N_p$ , into the corresponding flux linkage. Second, (6) is used to predict the flux linkage change. Following, (11b) is used to get  $\mathbf{i}_{dq}(k+\ell)$ . In doing so, the gradient calculation is improved noticeably. An illustrative example of the predicted and resulting error area is shown in Fig. 1, where the current trajectory computed with the inductance-based prediction model (3) (and thus based on the inductance  $L$ ) results in a suboptimal  $t_z$ , causing an unnecessary high current ripple, as compared with that computed with the proposed method. Finally, note that the nonlinear functions  $f_\psi$  and  $f_\psi^{-1}$  can either be approximated by analytical functions (high-degree polynomial) or stored in flux linkage maps. They can be identified, e.g., as shown in [10, p. 46]. In this work, flux linkage maps with linear interpolation are used, see Fig. 2.

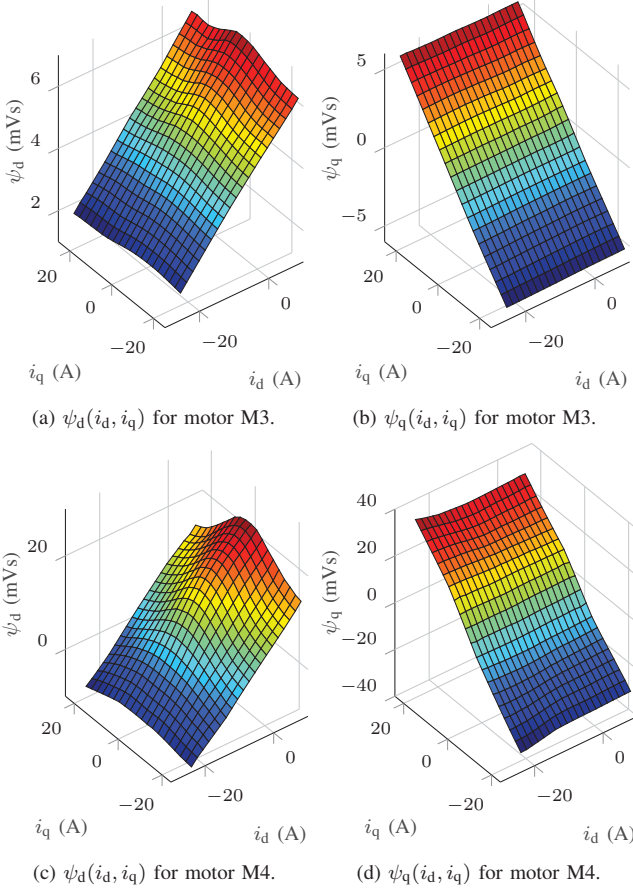


Figure 2. Identified flux linkage maps with 20x20 grid points.

#### D. Optimization Problem

The cost function, which decides whether zero, one, or two switching transitions occur, is chosen as

$$J(k) = \sum_{\ell=k}^{k+N_p-1} \left( \|\mathbf{y}^*(\ell+1) - \mathbf{y}(\ell+1)\|_2^2 + \hat{f}(\mathbf{i}_{dq}(\ell+1)) \right) + \lambda_u \|\Delta[\bar{\mathbf{u}}_{abc}^T(\ell-1) \bar{\mathbf{u}}_{abc}^T(\ell)]^T\|_1 \quad (12)$$

where

$$\hat{f}(\mathbf{i}_{dq}(\ell+1)) = \begin{cases} 4 & \text{if } \|\mathbf{i}_{dq}(\ell+1)\|_2 > i_{\max} \\ 0 & \text{if } \|\mathbf{i}_{dq}(\ell+1)\|_2 \leq i_{\max} \end{cases} \quad (13)$$

and the reference and output vectors being  $\mathbf{y}^* = [\mathbf{i}_{dq}^{*T} \mathbf{i}_{dq}^{*T}]^T \in \mathbb{R}^4$ , and  $\mathbf{y} = [\mathbf{i}_{dq,t_z}^T \mathbf{i}_{dq,T_{cf}}^T]^T \in \mathbb{R}^4$ , respectively. The switch positions are defined as  $\bar{\mathbf{u}}_{abc} = [\mathbf{u}_{abc,0}^T \mathbf{u}_{abc,t_z}^T]^T \in \mathbb{U}$  with  $\mathbb{U} = \{-1, 1\}^{N_p+1}$ . Moreover,  $\Delta[\bar{\mathbf{u}}_{abc}^T(\ell-1) \bar{\mathbf{u}}_{abc}^T(\ell)]^T$  with  $\Delta = \begin{bmatrix} \mathbf{0} & -\mathbf{I} & \mathbf{I} & \mathbf{0} \\ \mathbf{0} & \mathbf{0} & -\mathbf{I} & \mathbf{I} \end{bmatrix}$ , where  $\mathbf{0}$  and  $\mathbf{I}$  are the zero and identity matrices of corresponding dimensions (e.g.  $3 \times 3$ ), denotes the penalization of the control action, and, consequently, of the switching frequency, which is weighted by  $\lambda_u > 0$ . For computing the optimal SV(s), the predicted currents are inserted in (12) by taking into account the hard constraint (13), where “4” is the maximum current in per unit (p.u.).<sup>5</sup>

<sup>5</sup>Theoretically, a soft constraint is to be preferred since it can avoid feasibility problems when solving (12).

#### Algorithm 1 Flux linkage-based VSP<sup>2</sup>CC

```

1: function  $\bar{\mathbf{u}}_{ABC,OPT}, t_{z,OPT} = \psi\text{-VSP}^2\text{CC}(\mathbf{i}_{dq}, \varphi, N_p, \omega_{el}, V_{dc})$ 
2:    $\psi_{dq}(k-1) \leftarrow \mathbf{i}_{dq}(k-1)$  using (11a)
3:    $\psi_{dq}(k) \leftarrow$  predict using (6)  $\triangleright$  delay time comp.
4:    $\mathbf{i}_{dq}(k) \leftarrow \psi_{dq}(k)$  using (11b)
5:    $\mathbf{v}_{dq,db}(k) \leftarrow$  deadbeat sol.  $\triangleright$  search space reduction
6:    $\gamma(k) \leftarrow \angle \mathbf{v}_{dq,db}(k)$  using (7)  $\triangleright$  sector of  $\mathbf{v}_{dq}(k)$ 
7:   for  $\ell = 1, \dots, N_p$  do
8:      $\mathbf{v}_{dq}(k+\ell-1) \leftarrow$  based on  $\varphi(k+\ell-1)$  and  $V_{dc}(k)$ 
9:     for  $j = 1, \dots, 3$  do  $\triangleright$  one SV within  $T_{cf}$ 
10:       $\psi_{dq,j}(k+\ell) \leftarrow$  predict using (6)
11:       $\mathbf{i}_{dq,j}(k+\ell) \leftarrow \psi_{dq,j}(k+\ell)$  using (11b)
12:       $\|\mathbf{i}_{dq,j}(k+\ell)\| \leftarrow \mathbf{i}_{dq,j}(k+\ell)$  using (13)
13:      if  $\ell = 1$  then
14:         $\mathbf{m}_j(k+\ell) \leftarrow$  using (8)  $\triangleright \mathbf{i}_{dq}$  gradients
15:      end if
16:    end for
17:    if  $\ell = 1$  then  $\triangleright$  VSP for  $N_p = 1$ 
18:      for  $n_1 = 1, \dots, 3$  do
19:        for  $n_2 = 1, \dots, 3$  do
20:          if  $n_1 = n_2$  then  $\triangleright$  one SV within  $T_{cf}$ 
21:             $\mathbf{i}_{dq,n_1,n_2}(k+\ell) \leftarrow \mathbf{i}_{dq,j}(k+\ell)$ 
22:          else  $\triangleright$  VSP for two SVs
23:             $t_{z,n_1,n_2}(k+\ell) \leftarrow$  (10)  $\triangleright$  VSP
24:             $\psi_{dq,n_1,n_2}(k+\ell) \leftarrow$  pred. using (6)6
25:             $\mathbf{i}_{dq,n_1,n_2}(k+\ell) \leftarrow \psi_{dq,n_1,n_2}(k+\ell)$ 
26:             $\|\mathbf{i}_{dq,n_1,n_2}(k+\ell)\| \leftarrow \mathbf{i}_{dq,n_1,n_2}(k+\ell)$ 
27:          end if
28:        end for
29:      end for
30:    end if
31:     $\bar{\mathbf{u}}_{abc,opt}(k), t_{z,opt}(k) \leftarrow$  solve (12)
32:  end for
33: end function

```

In contrast to the cost function in [7], (12) adopts the squared  $\ell_2$ -norm for the tracking errors for stability and performance reasons [12]. In addition, since in case of IPMSMs the d-axis current is not controlled to zero, the current limit (13) is based on the amplitude of the stator current. Besides the above changes, the functionality of the proposed cost function is the same as that in [7], hence any redundant details are omitted.

#### E. Assessment of Influencing Factors

The proposed flux linkage-based prediction is particularly advantageous—as compared with [7]—for (small) drives with saturation and cross-coupling effects for the following reasons:

- The bigger  $R_{ph}$  is, e.g., for small motors (ironless winding), the bigger the voltage drop across it and the more significant the prediction error can get. Since the inductance appears in the denominator of (3), a decrease in it results in an underestimated voltage drop across  $R_{ph}$ .

<sup>6</sup>Theoretically, at time instant  $t_z$ , (11b) must be used to get  $\mathbf{i}_{dq,n_1,n_2}$  and  $\mathbf{i}_{q,n_1,n_2}$  so that the voltage drop over the resistance in the second part of the sampling interval is computed based on a more accurate current.

Table I  
MOTOR AND SYSTEM PARAMETERS IN THE LINEAR REGION

Description	Symbol	Motor M1 Bühler 1.25.058.401	Motor M3 ebm-papst ECI-63.20-K1-B00	Motor M4 Prototype
Rated torque	$T_N$	40 Ncm	42 Ncm	90 Ncm
Winding resistance	$R_{ph}$	0.07 $\Omega$	0.09 $\Omega$	0.29 $\Omega$
d-axis inductance	$L_d$	0.2 mH	0.18 mH	0.49 mH
q-axis inductance	$L_q$	0.2 mH	0.29 mH	2.10 mH
PM flux constant	$\psi_{PM}$	6.0 mVs	6 mVs	20 mVs
Pole pair number	$p$	4	4	4
dc-link voltage	$V_{dc}$	24 V	24 V	24 V

- The larger the ratio between  $L_d$  and  $L_q$ , the bigger the prediction error when saturation occurs.
- Due to the impact of  $\psi_{PM}$  (and by assuming a constant  $\vartheta_m$ ), the lower  $\omega_{el}$  is, the bigger the prediction error on the q-axis. The speed does not affect the d-axis error.
- The smaller the contribution of  $\psi_{PM}$  in  $\psi_d$  (stronger reluctance effect), the greater the prediction error on the q-axis.
- For a given PMSM and saturation, the smaller  $f_{cf}$  or the higher the dc-link voltage, the larger the prediction error.

The benefit of the proposed method is visualized in Fig. 1, where the negative impact due to wrongly predicted current trajectories is shown. As can be understood, if, e.g., the inductance is halved due to saturation, the resulting current is almost doubled since the electrical time constant  $\tau_{el}$  is halved.

#### IV. PERFORMANCE EVALUATION

The main advantage of VSP<sup>2</sup>CC was highlighted in [7]. In the sequel of the section, the performance of the proposed flux linkage-based VSP<sup>2</sup>CC is evaluated for three different motors, see Table I, through simulations and experiments. For all presented tests, a control interval of  $T_{cf} = 10 \mu s$  is used.

##### A. Simulation Results

First, the steady-state behavior of the commercial nonlinear motor M3 is tested, see Figs. 3 and 4. For comparison purposes, the performance with the  $L$ -VSP<sup>2</sup>CC approach [7] is also shown. As can be seen, the latter control method causes an unnecessarily high current ripple (see the measured current shown with a blue line) and—consequently—high THD ( $I_{THD}$ ) due to the poor prediction of  $t_z$  (see the predicted current shown with a light blue line). On the other hand, the proposed  $\psi$ -VSP<sup>2</sup>CC, which utilizes the flux linkage maps in Figs. 2(a) and 2(b), computes the VSP instant  $t_z$  such that the current ripple (red line)—and current THD—is significantly lower.

Further comparison of the steady-state performance—indicated by the THD—of the two approaches is shown in Table II for all three motors under consideration. For a fair comparison,  $\lambda_u$  is adjusted such that the two control algorithms operate the drives at an (almost) equal average switching frequency  $f_{sw}$  for each examined case. It is noteworthy that motor M1 shows identical behavior with both approaches due to its rather linear behavior. On the other hand, the performance improvement achieved with the proposed method is clearly highlighted with the prototype motor M4, which exhibits pronounced nonlinear behavior (see Figs. 2(c) and 2(d)).

Given the aforementioned results the following observations can be made. Owing to the fact that the proposed VSP<sup>2</sup>CC

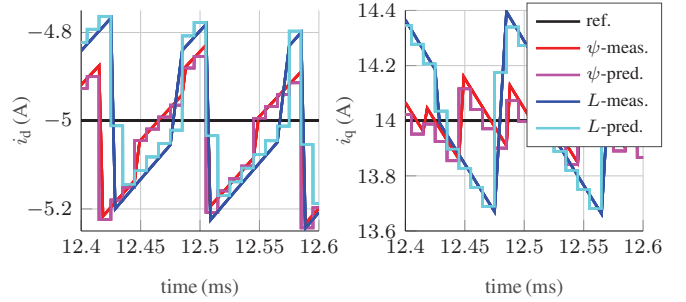


Figure 3. M3: VSP<sup>2</sup>CC at  $\angle\psi_{dq}=30^\circ$  with  $f_{sw}\approx 11.5$  kHz and  $n_m=100$  rpm.

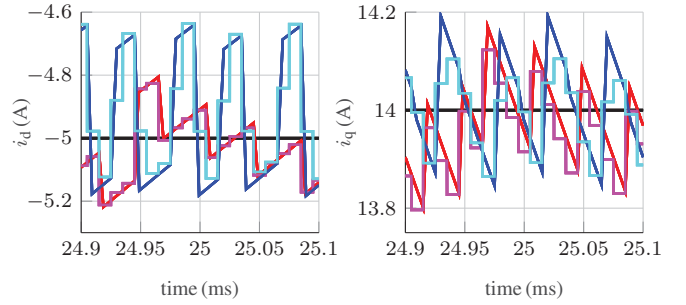


Figure 4. M3: VSP<sup>2</sup>CC at  $\angle\psi_{dq}=60^\circ$  with  $f_{sw}\approx 11.5$  kHz and  $n_m=100$  rpm.

Table II  
STATOR CURRENT THD FOR VSP<sup>2</sup>CC WHEN  $i_d^* = -5$  A AND  $i_q^* = 14$  A

Control method	$N_p$	$\lambda_u$	$n_m$ (rpm)	Simulation		Experiment	
				$f_{sw}$ (kHz)	$I_{THD}$ (%)	$f_{sw}$ (kHz)	$I_{THD}$ (%)
Motor M1							
$L$ -VSP <sup>2</sup> CC	2	0.045	100	9.55	0.94	9.6	1.5
$\psi$ -VSP <sup>2</sup> CC	2	0.045	100	9.55	0.94	9.6	1.5
$L$ -VSP <sup>2</sup> CC	2	0.112	2000	15.4	1.82	15.4	2.3
$\psi$ -VSP <sup>2</sup> CC	2	0.112	2000	15.4	1.81	15.4	2.3
Motor M3							
$L$ -VSP <sup>2</sup> CC	2	0.045	100	11.7	1.68	11.9	3.2
$\psi$ -VSP <sup>2</sup> CC	2	0.05	100	11.8	1.20	11.5	1.3
$L$ -VSP <sup>2</sup> CC	2	0.074	2000	17.3	2.30	17.1	4.0
$\psi$ -VSP <sup>2</sup> CC	2	0.15	2000	16.8	1.98	16.9	2.1
$L$ -VSP <sup>2</sup> CC	5	0.09	2000	16.2	2.18	—	—
$\psi$ -VSP <sup>2</sup> CC	5	0.15	2000	16.2	1.86	—	—
Motor M4							
$L$ -VSP <sup>2</sup> CC	2	0.02	200	8.9	1.41	10.1	6.0
$\psi$ -VSP <sup>2</sup> CC	2	0.02	200	7.8	0.63	9.9	1.7
$L$ -VSP <sup>2</sup> CC	2	0.045	200	5.15	1.87	5.1	8.5
$\psi$ -VSP <sup>2</sup> CC	2	0.05	200	5.1	0.91	4.9	2.1

method accounts for saturation and cross-coupling, its advantages are more evident when the machine is strongly nonlinear, especially for operation at low speeds. Regarding the latter, the effective computation of the VSP can have a significant impact on ripple reduction, see Fig. 1, due to the less frequent switching. Moreover, as can be seen in the flux linkage maps in Figs. 2(a)-2(b), the saturation effect is more dominant on the q- than the d-axis. Since for the chosen case studies the q-component of the required current prevails ( $|i_q^*| > |i_d^*|$ ), when the q-axis is aligned with a discrete voltage SV, a suboptimal prediction has a stronger adverse effect on the system performance. This implies that  $L$ -VSP<sup>2</sup>CC will result in an increased current ripple at the middle of each sector, as can be seen in Figs. 3 to 5. Further, from Table II it can be deduced that a constant  $\lambda_u$  for the whole speed range would result in less switching (and losses) at low speed—and vice

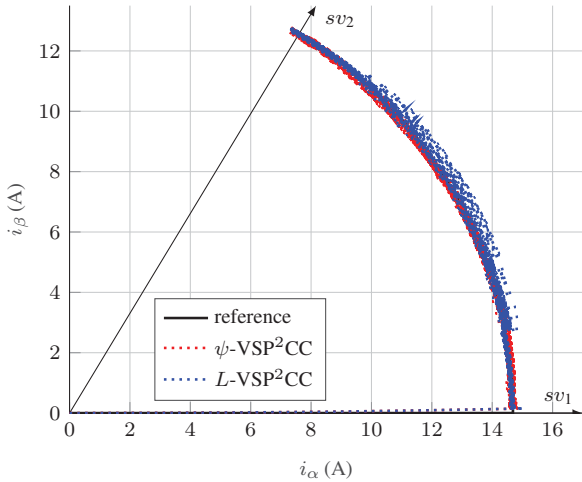


Figure 5. Motor M3: Current for the first sector with  $i_d^* = -5$  A,  $i_q^* = 14$  A at steady-state with  $f_{sw} \approx 11.5$  kHz and a speed of  $n_m = 100$  rpm.

versa at high speed—which is advantageous for drives. Finally, as confirmed in Table II, the THD decreases as the prediction horizon increases [2]. This comes with other benefits, such as improved stability, effective minimization of the steady-state error, and the ability to prioritize the d-axis error during transients for improved dynamic performance.

### B. Experimental Results

The proposed algorithm is implemented on the FPGA of a Zynq-7000 (XC7Z020) SoC, using the HDL-Coder from MathWorks, as described in [1], [7]. The processor is used for the parametrization of the MPC algorithm (i.e.,  $R_{ph}$ , flux linkage maps,  $\lambda_n$ ) and the communication. The FPGA implementation is advantageous, since high clock frequencies can be used for both parallel and serial calculations. For an efficient implementation, resource streaming is used for the for-loops and the flux linkage maps. The sampling/current control frequency is  $f_{cf} = 100$  kHz. In addition, since divisions are not efficient in FPGAs, the calculation of the denominator in (6) is done on the processor with  $f_{cc} = 10$  kHz.<sup>7</sup> Fig. 6 shows the phase current for two different operating points using  $L$ - and  $\psi$ -VSP<sup>2</sup>CC, respectively, with  $N_p = 2$ . An increasing reference causes saturation and as a consequence an increased current ripple and THD for  $L$ -VSP<sup>2</sup>CC. The THD of M4 in Table II shows a big difference between simulation and experiment. The prototype motor M4 has pronounced current harmonics, i.e. 5<sup>th</sup> and 7<sup>th</sup>, which are neither respected in the flux linkage maps nor in the inductances so far.

### V. CONCLUSION

In this paper, an extension of the VSP<sup>2</sup>CC algorithm was presented which uses the flux linkage instead of inductances for the prediction of the current trajectory. With the proposed method, nonlinear effects, such as saturation and cross-coupling, present in IPMSMs are taken into account and fully respected. In so doing, more accurate predictions of the current slopes are enabled which result in a more effective calculation

<sup>7</sup>Theoretically, when using VSP<sup>2</sup>CC at high speeds  $T_{cf}t_z$ —instead of  $T_{cf}$ —should be used in the denominator of (6) for the prediction up to the VSP instant and  $T_{cf} - T_{cf}t_z$  for the second part of the interval.

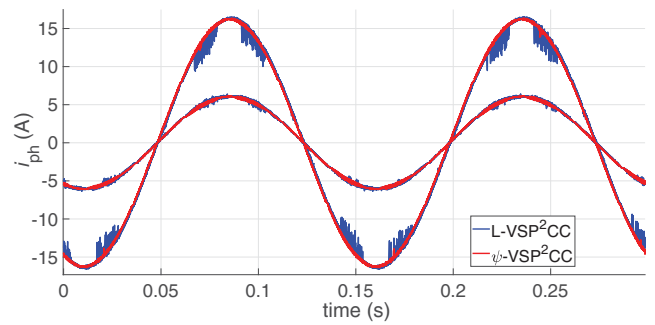


Figure 6. Motor M3: Single-phase stator current with  $i_d^* = -0.5$  A,  $i_q^* = 16$  A at  $n_m = 100$  rpm with  $I_{THD} = 5.5\%$  for  $L$ - and  $1.4\%$  for  $\psi$ -VSP<sup>2</sup>CC at  $f_{sw} \approx 12$  kHz. For comparison, an operating point without saturation, i.e.,  $i_d^* = -0.5$  A,  $i_q^* = 6$  A, is shown.

of the VSPs, i.e., the time instants where a new voltage SV is applied to the converter. Consequently, the current ripples, and thus the THD, are significantly reduced, indicating an improvement in the drive performance. In addition, the flux linkage maps can be used for efficient torque utilization. Future work includes the rotor position dependency and iron loss effects to increase the prediction accuracy of VSP<sup>2</sup>CC.

### REFERENCES

- [1] S. Wendel, A. Dietz, and R. Kennel, "FPGA based finite-set model predictive current control for small PMSM drives with efficient resource streaming," in *Proc. IEEE Int. Symp. Pred. Control Elect. Drives Power Electron.*, Pilsen, Czech Republic, Sep. 2015, pp. 66–71.
- [2] P. Karamanakos and T. Geyer, "Guidelines for the design of finite control set model predictive controllers," *IEEE Trans. Power Electron.*, vol. 35, no. 7, pp. 7434–7450, Jul. 2020.
- [3] P. Karamanakos, P. Stolze, R. M. Kennel, S. Manias, and H. du Toit Mouton, "Variable switching point predictive torque control of induction machines," *IEEE J. Emerg. Sel. Topics Power Electron.*, vol. 2, no. 2, pp. 285–295, Jun. 2014.
- [4] P. Stolze, P. Karamanakos, M. Tomlinson, R. Kennel, T. Mouton, and S. Manias, "Heuristic variable switching point predictive current control for the three-level neutral point clamped inverter," in *Proc. IEEE Int. Symp. Pred. Control Elect. Drives Power Electron.*, Munich, Germany, Oct. 2013.
- [5] L. Tarisciotti, P. Zanchetta, A. Watson, J. C. Clare, M. Degano, and S. Bifaretti, "Modulated model predictive control for a three-phase active rectifier," *IEEE Trans. Ind. Appl.*, vol. 51, no. 2, pp. 1610–1620, Mar./Apr. 2015.
- [6] Y. Zhang, W. Xie, Z. Li, and Y. Zhang, "Low-complexity model predictive power control: Double-vector-based approach," *IEEE Trans. Ind. Electron.*, vol. 61, no. 11, pp. 5871–5880, Nov. 2014.
- [7] S. Wendel, P. Karamanakos, A. Dietz, and R. Kennel, "Operating point dependent variable switching point predictive current control for PMSM drives," in *Proc. IEEE Int. Symp. Pred. Control Elect. Drives Power Electron.*, Quanzhou, China, May/June 2019.
- [8] J. Richter, T. Gemaßmer, and M. Doppelbauer, "Predictive current control of saturated cross-coupled permanent magnet synchronous machines," in *Proc. Int. Symp. on Power Electron., Elect. Drives, Autom. and Motion*, Ischia, Italy, Jun. 2014, pp. 830–835.
- [9] B. Štumberger, G. Štumberger, D. Dolinar, A. Hamler, and M. Trlep, "Evaluation of saturation and cross-magnetization effects in interior permanent-magnet synchronous motor," *IEEE Trans. Ind. Appl.*, vol. 39, no. 5, pp. 1264–1271, Sep./Oct. 2003.
- [10] J. Richter, "Modellbildung, Parameteridentifikation und Regelung hoch ausgenutzter Synchronmaschinen," Ph.D. dissertation, Fakultät für Elektrotechnik und Informationstechnik, Karlsruhe Institute of Technology, Karlsruhe, Germany, 2016.
- [11] J. Germishuizen and R. Tanner, "Stepped versus fixed rotor position FEA solutions for 2D flux linkage maps in machine design," in *Proc. Int. Conf. on Elect. Mach.*, Alexandroupoli, Greece, Sep. 2018, pp. 982–987.
- [12] P. Karamanakos, T. Geyer, and R. Kennel, "On the choice of norm in finite control set model predictive control," *IEEE Trans. Power Electron.*, vol. 33, no. 8, pp. 7105–7117, Aug. 2018.